Swept source optical coherence tomography as a tool for real time visualization and localization of electrodes used in electrophysiological studies of brain *in vivo*

Hideyuki Watanabe,[1,4] Uma Maheswari Rajagopalan,[4] Yu Nakamichi,[4] Kei M. Igarashi,[2,3,4] Hirofumi Kadono,[1] and Manabu Tanifuji[4,*]

[1]*Graduate School of Science and Engineering, Saitama University, 255 Shimo-Okubo, Sakura-ku, Saitama-city, Saitama, 338-08570, Japan*

[2]*Centre for the Biology of Memory, Medical-Technical Research Centre Norwegian University of Science and Technology, Olav Ktrres gate 9, 7030 Trondheim, Norway*

[3]*Department of Physiology, Graduate of Medicine, University of Tokyo, 7-3-1 Hongo, Bunkyo-ku, Tokyo, 113-0033 Japan*

[4]*Laboratory for Integrative Neural Systems, RIKEN Brain Science Institute, 2-1 Hirosawa, Wako-city, Saitama, 351-0198, Japan*

**tanifuji@riken.jp*

Abstract: In studies of *in vivo* extracellular recording, we usually penetrate electrodes almost blindly into the neural tissue, in order to detect the neural activity from an expected target location at a certain depth. After the recording, it is necessary for us to determine the position of the electrodes precisely. Generally, to identify the position of the electrode, one method is to examine the postmortem tissue sample at micron resolution. The other method is using MRI and it does not have enough resolution to resolve the neural structures. To solve such problems, we propose swept source optical coherence tomography (SS-OCT) as a tool to visualize the cross-sectional image of the neural target structure along with the penetrating electrode. We focused on a rodent olfactory bulb (OB) as the target. We succeeded in imaging both the OB layer structure and the penetrating electrode, simultaneously. The method has the advantage of detecting the electrode shape and the position in real time, *in vivo*. These results indicate the possibility of using SS-OCT as a powerful tool for guiding the electrode into the target tissue precisely in real time and localizing the electrode tip during electrophysiological recordings.

OCIS codes: (170.3880) Medical and biological imaging; (170.4500) Optical coherence tomography; (170.5380) Physiology

References and links

1. A. L. Fantana, E. R. Soucy, and M. Meister, "Rat olfactory bulb mitral cells receive sparse glomerular inputs," Neuron **59**(5), 802–814 (2008).
2. S. Nagayama, Y. K. Takahashi, Y. Yoshihara, and K. Mori, "Mitral and tufted cells differ in the decoding manner of odor maps in the rat olfactory bulb," J. Neurophysiol. **91**(6), 2532–2540 (2004).
3. E. R. Griff, M. Mafhouz, A. Perrut, and M. A. Chaput, "Comparison of identified mitral and tufted cells in freely breathing rats: I. Conduction velocity and spontaneous activity," Chem. Senses **33**(9), 779–792 (2008).
4. J. Chapuis, S. Garcia, B. Messaoudi, M. Thevenet, G. Ferreira, R. Gervais, and N. Ravel, "The way an odor is experienced during aversive conditioning determines the extent of the network recruited during retrieval: a multisite electrophysiological study in rats," J. Neurosci. **29**(33), 10287–10298 (2009).
5. T. Sato, G. Uchida, and M. Tanifuji, "Cortical columnar organization is reconsidered in inferior temporal cortex," Cereb. Cortex **19**(8), 1870–1888 (2009).
6. D. Huang, E. A. Swanson, C. P. Lin, J. S. Schuman, W. G. Stinson, W. Chang, M. R. Hee, T. Flotte, K. Gregory, C. A. Puliafito, and J. G. Fujimoto, "Optical coherence tomography," Science **254**(5035), 1178–1181 (1991).
7. M. Wojtkowski, "High-speed optical coherence tomography: basics and applications," Appl. Opt. **49**(16), D30–D61 (2010).
8. W. Drexler and J. G. Fujimoto, eds., *Optical Coherence Tomography* (Springer-Verlag, 2008).

#153307 - $15.00 USD Received 24 Aug 2011; revised 14 Oct 2011; accepted 20 Oct 2011; published 25 Oct 2011

9. B. E. Bouma and G. J. Tearney, eds., *Handbook of Optical Coherence Tomography* (Marcel Dekker, 2002).
10. W. Suzuki, G. Hanazono, T. Nanjo, K. Ito, J. Nishiyama, M. Tanifuji, and K. Tsunoda, "Intrinsic signals in different layers of macaque retina revealed by optical coherence tomography (OCT)," Abstr. Soc. Neurosci. 171.19 (2010).
11. R. U. Maheswari, H. Takaoka, H. Kadono, R. Homma, and M. Tanifuji, "Novel functional imaging technique from brain surface with optical coherence tomography enabling visualization of depth resolved functional structure in vivo," J. Neurosci. Methods **124**(1), 83–92 (2003).
12. Y. Chen, A. D. Aguirre, L. Ruvinskaya, A. Devor, D. A. Boas, and J. G. Fujimoto, "Optical coherence tomography (OCT) reveals depth-resolved dynamics during functional brain activation," J. Neurosci. Methods **178**(1), 162–173 (2009).
13. S. R. Chinn, E. A. Swanson, and J. G. Fujimoto, "Optical coherence tomography using a frequency-tunable optical source," Opt. Lett. **22**(5), 340–342 (1997).
14. M. A. Choma, M. V. Sarunic, C. Yang, and J. A. Izatt, "Sensitivity advantage of swept source and Fourier domain optical coherence tomography," Opt. Express **11**(18), 2183–2189 (2003).
15. H. Watanabe, U. M. Rajagopalan, Y. Nakamichi, K. M. Igarashi, V. D. Madjarova, H. Kadono, and M. Tanifuji, "In vivo layer visualization of rat olfactory bulb by a swept source optical coherence tomography and its confirmation through electrocoagulation and anatomy," Biomed. Opt. Express **2**(8), 2279–2287 (2011).
16. W. R. Chen, J. Midtgaard, and G. M. Shepherd, "Forward and backward propagation of dendritic impulses and their synaptic control in mitral cells," Science **278**(5337), 463–467 (1997).
17. H. Matsumoto, H. Kashiwadani, H. Nagao, A. Aiba, and K. Mori, "Odor-induced persistent discharge of mitral cells in the mouse olfactory bulb," J. Neurophysiol. **101**(4), 1890–1900 (2009).
18. K. Zhang and J. U. Kang, "Real-time 4D signal processing and visualization using graphics processing unit on a regular nonlinear-*k* Fourier-domain OCT system," Opt. Express **18**(11), 11772–11784 (2010).
19. S. A. Boppart, "Optical coherence tomography: technology and applications for neuroimaging," Psychophysiology **40**(4), 529–541 (2003).
20. M. Lalancette-Hébert, D. Phaneuf, G. Soucy, Y. C. Weng, and J. Kriz, "Live imaging of Toll-like receptor 2 response in cerebral ischaemia reveals a role of olfactory bulb microglia as modulators of inflammation," Brain **132**(4), 940–954 (2009).
21. S. Breit, J. B. Schulz, and A. L. Benabid, "Deep brain stimulation," Cell Tissue Res. **318**(1), 275–288 (2004).

1. Introduction

Recording neural activity and stimulation of specific neural elements such as neurons with microelectrodes are major methods for investigating neural systems in electrophysiology [1,2]. Generally, in such studies, the penetration of the electrodes has been performed rather blindly to reach an expected specific location by using the stereotactic coordinates as the reference coordinates [2,3]. It is necessary for us to use either MRI or to examine the postmortem tissue sample [4,5] in order to determine the precise position of the electrode at the specific target. However, MRI does not support a few micrometer level of spatial resolution in localizing the electrode. In the case of postmortem tissue slicing, it is difficult to confirm the location of the electrode, *in vivo*.

As a complementary technique, we employed optical coherence tomography (OCT) [6–12]. Practically, we introduced a swept source optical coherence tomography (SS-OCT) [13,14] as a tool for localization of the electrode to the neural tissue, *in vivo*. In general, OCT has the advantage of imaging at micrometer spatial resolutions in both lateral and depth directions, a high temporal resolution of a few microseconds for single A-scan, and an imaging depth up to a few millimeters. Further, SS-OCT is robust to motion as SS-OCT uses a high-speed point detector. In our previous study that focused on a rat olfactory bulb (OB) as a biological target tissue, we succeeded in visualizing OB neural layer structures *in vivo* by using SS-OCT as shown in Fig. 1. In that study, we confirmed that the layer structures of OB correspond to distinctive important anatomical neural layers by using electrocoagulation [15].

In this study, we propose SS-OCT as a tool for real time monitoring of electrode penetration and localization of the electrode to the specific target neural layer, *in vivo*. MCL has been regarded as one of the important regions for understanding OB mechanism. MCL has been studied by electrophysiological methods with electrode. Therefore, in this study, we chose MCL (mitral cell body layer) as our specific target layer [1,2,16,17].

#153307 - $15.00 USD Received 24 Aug 2011; revised 14 Oct 2011; accepted 20 Oct 2011; published 25 Oct 2011

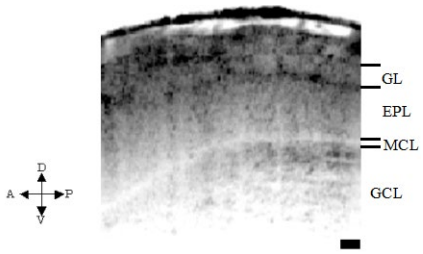

Fig. 1. Neural layer structure of OB imaged by using SS-OCT. OB consists of distinctive different layers, namely: glomerulous layer (GL), external plexiform layer (EPL), mitral cell body layer (MCL) and granule cell layer (GCL). Here, we choose MCL as our specific target layer that is known to contain mainly cell bodies from which extracellular recordings are usually done. The arrows on the left corner indicate the anterior-posterior and dorsal-ventral parts of the rat. A, anterior; P, posterior; D, dorsal; V, ventral. Scale bar, 100 μm.

2. Experimental details

2.1. Experimental system

We introduced a custom made SS-OCT system (Santec corporation, Aichi, Japan) that uses a swept laser source (Santec, HSL-2000) having a center wavelength 1334 nm with a full width half maximum (FWHM) 117 nm and providing an average output power of 18.1 mW. The imaging depth in air was 2.9 mm at least. The theoretical values for depth and lateral resolutions are 6.7 μm and 15.4 μm, respectively. The signal noise ratio was 66.6 dB with using mirror. Scanning speed of the swept source laser was 20 kHz. The details of the interferometer system were described in our previous study [15].

The probe part consisted of two components. One was the optical probe unit of the SS-OCT system mounted on an independent universal stand (Olympus, SZ2-STU2) with a focusing unit (Olympus, BXFM-F), and the other was the electrode penetration probe unit.

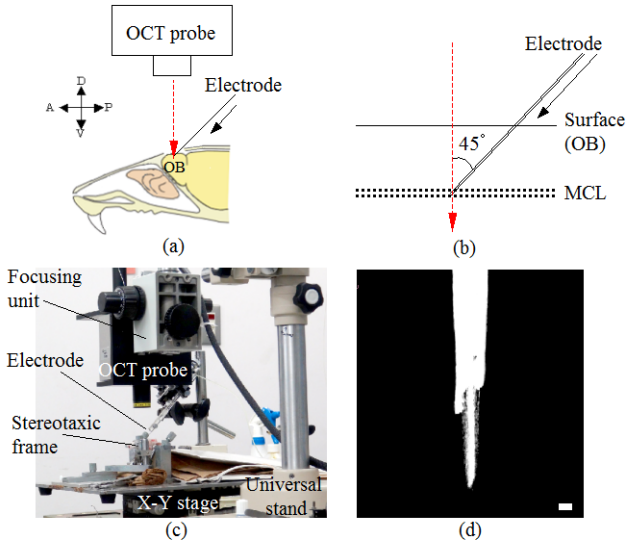

Fig. 2. (a) A schematic view of the olfactory bulb (OB) with an electrode penetration and the OCT probe unit. The arrows on the left corner indicate the anterior-posterior and dorsal-ventral parts of the rat. A, anterior; P, posterior; D, dorsal; V, ventral. (b) A schematic of the magnified view of the electrode into mitral cell body layer (MCL) of OB. The angle between the optical axis and the electrode was set to be approximately 45 degree. (c) An optical micrograph of the optical probe unit of SS-OCT and the electrode probe unit. (d) An optical micrograph of the electrode with the external insulator seen as white and the exposed tungsten electrode seen rather as gray with the scale bar corresponding to 50 μm.

#153307 - $15.00 USD Received 24 Aug 2011; revised 14 Oct 2011; accepted 20 Oct 2011; published 25 Oct 2011

The latter unit was mounted on an X-Y micrometer stage (Chuo-Seiki, LD-131-S1), along with a stereotactic frame for fixing the animal. The whole arrangement enabled us to adjust the relative position of the probe units independently. Further, as the rat and the electrode probe unit were moved by X-Y micrometer stage, it was possible to keep the relative spatial position. By using the rotatable focusing unit attached to the stand, it was possible for us to adjust the plane of the OCT image to the plane of the electrode penetration.

The surface of OB was perpendicularly illuminated by the sample beam of the OCT system. The electrode was penetrated at an angle of 45 degree to the optical axis of the sample beam (Figs. 2(a)–2(c)). The electrode was the same as that used in our previous electrocoagulation studies [15]. The tungsten electrode was covered with an insulator seen as the white region in Fig. 2(d) having a diameter of around 130 μm. The tungsten electrode had a tapered structure, and it was exposed by stripping off the insulator. The exposed region had a length of 280 μm from the tip. The diameter of the tungsten electrode at the boundary between the outer insulator and the stripped electrode was 60 μm while the tip had a diameter of 10μm (Fig. 2(d)). The electrode was translated by using a stepping motor microdrive (Narishige, PC5N). The plane of electrode penetration was adjusted to be the same as the cross sectional plane of the OCT imaging.

2.2. Animal preparation details

The animal details were almost the same as our previous work [15]. A Sprague-Dawley rat (SLC Japan, 8weeks, 287g) was anesthetized with medetomidine hydrochloride (Orion, Domitor, 0.05ml/100g i.m.) and ketamine hydrochloride (Daiichi-Sankyo, Ketalar, 0.15ml/100g i.p.). The body temperature was maintained at 36.5 degrees Celsius with a temperature controlled heat blanket (Nihon Kohden, ATB-1100). The heartbeat was continuously monitored during experiment by a heart rate counter equipped with a bioelectric amplifier (Nihon Kohden, AT-601G and AB-621G). The rat was mounted on a stereotactic frame with an ear-bar set. Only the dorsal right OB region was exposed after removing the skull with a dental drill and covered with mineral oil. During the experiments, we kept the heart rate of the animal to be around 260 beats/min. The experimental protocol was approved by the Animal Experiments Committee of RIKEN that follows the guideline of the National Institute of Health.

3. Result and discussion

3.1. Monitoring of electrode penetration to the neural layer structure

Figure 3 shows raw OCT B-scan images obtained at different times during the penetration. We identified the electrode penetration process in real time. Due to the electrode being metal that has a strong OCT reflectivity, the electrode invariably casts a shadow underneath obstructing the view of the entire imaging depth. We also identified the blood vessel structure and the shadow cast below as in our previous study (refer to Fig. 4(c) of [15]). The penetration process of the electrode into OB reaching up to the target location of MCL was seen. The penetration process was presented in the attached movie of raw images. The movie was made in mpeg format at twice the speed of 30 frames per second (fps) from the original frame rate of 15 fps. The limitation on the original frame rate came from both the hardware and the software limitations such as the scanning speed, FFT conversion, processing of monitoring output in real time and data transfer from onboard memory of A/D converter to the computer's main memory. The data copy from the main memory to the hard disk was performed simultaneously by using another thread loop. In addition, in the raw image as well as in the movie, we saw granular structures corresponding to the speckles appearing as a result of multiple scattering within the probing coherence volume and thus decreasing the image quality.

In order to reduce speckles, Fig. 4 shows 5-frame averaged OCT B-scan images obtained at different times during the penetration. The original data set was exactly same as shown in Fig. 3. Frame averaging clearly reduced the speckle noise. Here, we used linear scale for the

#153307 - $15.00 USD Received 24 Aug 2011; revised 14 Oct 2011; accepted 20 Oct 2011; published 25 Oct 2011

calculation of averaging and then converted to logarithmic scale for display purposes to have enough dynamic range.

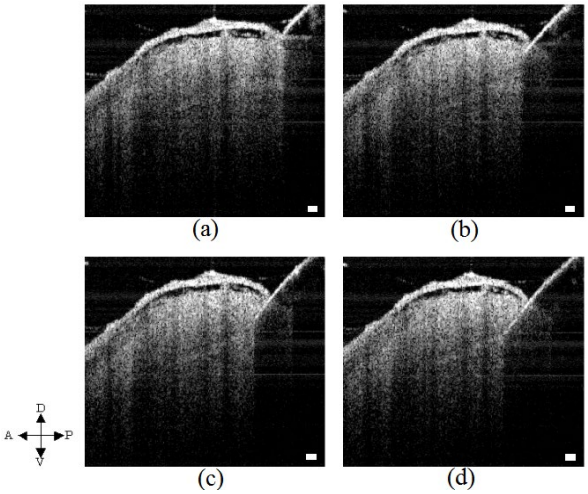

Fig. 3. Raw OCT B-scan images obtained during the electrode penetration process at different times (a) t = 0, (b) t = 7, (c) t = 10.5, and (d) t = 14 sec. The penetration process was monitored and finally reaching the target location of MCL. We saw granular structure corresponding to speckles appearing as a result of multiple scattering within the probing coherence volume. The arrows on the left corner indicate the anterior-posterior and dorsal-ventral parts of the rat. A, anterior; P, posterior; D, dorsal; V, ventral. Scale bar, 100 μm. Refer to the movie (Media 1) of raw images.

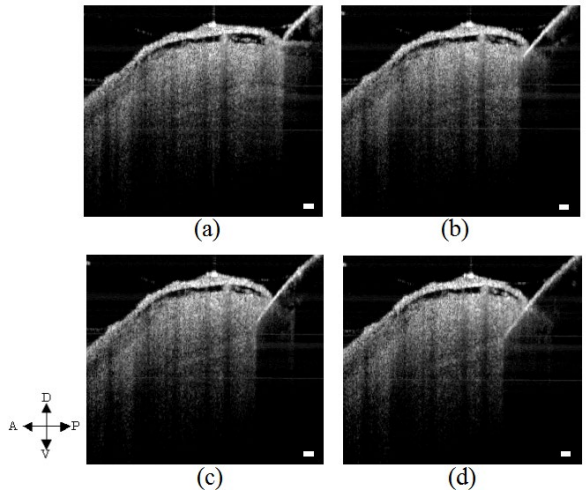

Fig. 4. Five-frame averaged OCT B-scan images obtained during the electrode penetration process at different times (a) t = 0 sec; (b) t = 7 sec; (c) t = 10.5 sec; (d) t = 14 sec. The penetration process was clearly seen and finally reaching the target location of MCL. The arrows on the left corner indicate the anterior-posterior and dorsal-ventral parts of the rat. A, anterior; P, posterior; D, dorsal; V, ventral. Scale bar, 100 μm. Refer to the movie (Media 2) of five-frame averaged images.

3.2 Localization of the electrode to the neural layer structure

When the electrode reached the target layer of MCL, the penetration was stopped, we took 50,000 B-scan images of OCT images. The B-scan images were corrected for any misalignment due to the movement of the brain through the process of cross-correlation. After

#153307 - $15.00 USD Received 24 Aug 2011; revised 14 Oct 2011; accepted 20 Oct 2011; published 25 Oct 2011

that, all frames were averaged. Further, in order to reduce the artifacts of vertical shadow in the axial direction due to the vessels in the OCT images, we performed normalization of each vertical line by using the standard deviation of each A-scan OCT signal. The normalization process made the identification and the localization of the electrode easier and clearer. We succeeded in localizing the electrode at the MCL neural layer structure of OB *in vivo* in Fig. 5(a). Figure 5(b) was shown for clarity as an inverted intensity map of Fig. 5(a). As the tip diameter was almost close to the resolution limits of the SS-OCT system, the OCT signal was weak. It was necessary to increase the number of averaging of OCT images to improve the contrast of the image in identifying both the tip and the target location as shown in Fig. 5.

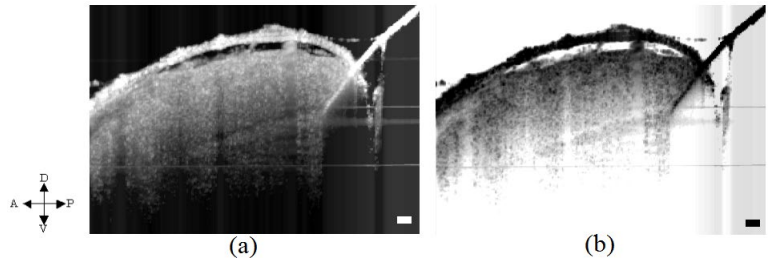

Fig. 5. (a) Averaged OCT B-scan image of OB with the stationary electrode being positioned at the target location MCL of OB. (b) Averaged OCT image same as (a) with inverted dynamic range to have a clear visualization of the target layer in relation to the electrode. Part below the electrode in the OCT signal was not detectable because the electrode practically reflected the sample beam. The arrows on the left corner indicate the anterior-posterior and dorsal-ventral parts of the rat. A, anterior; P, posterior; D, dorsal; V, ventral. Scale bar, 100 μm.

4. Summary

So far, the penetration of the electrodes has usually been performed rather blindly to the specific location by using the stereotactic coordinates, and it was necessary to inspect the postmortem slices for confirmation of the electrode after recording. To solve this problem, we showed that SS-OCT works as a tool to visualize and localize the electrode at the specific location of neural layer structure of OB under real time. We also showed that our proposed real time visualization of electrode by SS-OCT eliminates the necessity for confirmation through postmortem slice investigations.

In the current system, real time frame rate was limited by the signal processing, for instance FFT calculation. However, with the availability of the latest high-end hardware processing tools such as graphics processing unit (GPU), digital-signal-processing (DSP) and field programmable gate array (FPGA) [18,19], we expect processing speed to increase dramatically.

We believe, our approach is not only restricted to electrode penetration studies *in vivo* but also to microinjection experiments in neural layer structure where we inject small amount of foreign materials into the target location such as in anatomical tracing and local virus expression [20]. With the current system, there exists another possibility of using the system as a position-tracking tool for endoscopes (also OCT endoscopes). We also hope that a combination tool of SS-OCT with the conventional ones such as MRI, CT or cerebral ventriculography [21] may help in contributing to the study of brain diseases such as Parkinson's disease.

Acknowledgments

We thank Mr. Takayuki Sato for his advice on electrode penetration. We would like to thank the staff members of Research Resources Center in taking care of the animals. We also thank Mr. Atsushi Morosawa and Mr. Takuya Suzuki of Santec Corporation (Aichi, Japan) for their technical assistance in customizing the SS-OCT system.

#153307 - $15.00 USD Received 24 Aug 2011; revised 14 Oct 2011; accepted 20 Oct 2011; published 25 Oct 2011